SCIENTIFIC REPORTS

OPEN

SUBJECT AREAS:
CERAMICS
ENVIRONMENTAL CHEMISTRY

Received
21 March 2014

Accepted
7 August 2014

Published
29 October 2014

Correspondence and requests for materials should be addressed to C.-A.W. (wangca@tsinghua.edu.cn)

Multi-Enhanced-Phonon Scattering Modes in Ln-Me-A Sites co-substituted $LnMeA_{11}O_{19}$ Ceramics

Haoran Lu[1], Chang-An Wang[1], Yong Huang[1] & Huimin Xie[2]

[1]State Key Lab of New Ceramics and Fine Processing, School of Materials Science and Engineering, Tsinghua University, Beijing 100084 (P. R. China), [2]School of Aerospace Engineering, Tsinghua University, Beijing 100084 (P. R. China).

Authors reported an effective path to decrease the thermal conductivity while to increase the coefficient of thermal expansion, thus enhancing the thermo-physical properties of the $LnMeA_{11}O_{19}$-type magnetoplumbite $LaMgAl_{11}O_{19}$ by simultaneously substituting La^{3+}, Mg^{2+} and Al^{3+} ions with large ionic radius Ba^{2+}, Zn^{2+} and Ti^{4+}, respectively. The mechanism behind the lowered thermal conductivity was mainly due to the multi-enhanced-phonon scattering modes in Ln-Me-A sites co-substituted $LnMeA_{11}O_{19}$ ceramics. These modes involve the following four aspects, namely, point defect mechanism, the intrinsic scattering in the complex crystal cell and materials with stepped surface to localize phonon vibrational modes, as well as nano-platelet-like structure to incorporate additional grain boundary scattering. This study provides novel thoughts for promising candidate materials of even lower thermal conductivity for the next generation thermal barrier coatings.

Thermal barrier coatings (TBCs) have attracted extensive interest owing to their wide applications in the areas of coat transition pieces, combustion lines, first stage blades and vanes, as well as hot-path components of gas turbines. In addition to high melting points, absence of phase transformation from room temperature to the operating temperature, chemical inertness, low sintering rate and thermal expansion perfectly matching the substrate, low thermal conductivity is the most valuable characteristics to be considered. The total theoretical thermal conductivity of polycrystalline ceramics is simply the sum of the followed two terms[1–3]:

$$\kappa = \kappa_p + \kappa_r = \frac{1}{3}\int C_v \rho v m l_p + \frac{16}{3}\sigma n^2 T^3 l_r \tag{1}$$

where κ_p and κ_r are the thermal conductivities contributed by vibrations and radiation, respectively, C_v is the specific heat capacity at constant volume, ρ is the density of the material, v_m is the mean velocity of phonons in the material, l_p is the phonon mean free path, σ is Stefan Boltzmann's constant (5.67×10^{-8} $W \cdot m^{-2} \cdot K^{-1}$), n is the refractive index of the material, T and l_r are the thermodynamic temperature (K) and photon mean free path, respectively. The specific heat capacity at constant volume for any crystalline solids at a value of $3Nk_B \approx 25$ $J \cdot mol^{-1} \cdot K^{-1}$ above the Debye temperature. Therefore to lower the thermal conductivity in TBCs ceramics, the main approaches are to lower ρ, v_m or l_p. The total phonon mean free path, in TBCs ceramics, is primarily defined by:

$$l_p^{-1} = l_i^{-1} + l_{vac}^{-1} + l_{gb}^{-1} + l_{point}^{-1} + l_{ls}^{-1} \tag{2}$$

where l_i is the intrinsic mean free path of phonons due to the difference among ion masses, l_{vac}, l_{gb}, l_{point} and l_{ls} are the mean free path of phonons contributed by vacancies, grain boundaries, point defects and layered microstructures, respectively. The designs to reduce l_p has been engineered on several types of oxide ceramics, intermetallic compounds or metal chalcogenides (e.g. $La_2Zr_2O_7$[4], 7-8YSZ[5,6], $LaMgAl_{11}O_{19}$[7,8], W/Al_2O_3[9], PbTe–$PbSnS_2$[10]) by separately introducing point defects, vacancies, complex crystal structures, nanosized grains and layered microstructures. However, there is insufficient research into realizing above-mentioned scattering mechanisms jointly working in one TBCs material system, and materials meeting these requirements are not easily synthesized in the laboratory.

Recently, some researchers have reported experimentally that nano-grain boundaries[11,12], point defects[13] and layered microstructure[10,14] play important roles in enhancing the phonon scattering. Focusing on the role of

combined phonon scattering mechanisms on the thermal conductivity, we note that $LnMeA_{11}O_{19}$[15–17] (Figure S1, Supplementary information) has been proposed as one of promising candidates for the next generation thermal barrier coatings[18]. However, doping-free $LaMgAl_{11}O_{19}$ still shows relatively high thermal conductivity, rendering it harder to achieve smaller phonon mean free path. While introducing point defects has been proved to be an effective approach to reduce thermal conductivity of materials with exeptionally low κ. Furthermore, multi-sites-doping is a successful strategy to introduce multi-sites distortion and disorder with mass and strain fluctuations. In addition, smaller grain size resulting in a higher number of grain boundaries in the heat path adds additional thermal resistance to the polycrystalline solid phase. Therefore, it is significantly attractive to evaluate and characterize the thermo-physical properties of Ln-Me-A sites co-substituted $LnMeA_{11}O_{19}$ ceramics with nanosized grains and thereby to seek a novel thought to further lower thermal conductivity.

In this study, we optimized the κ of the $LnMeA_{11}O_{19}$-type magnetoplumbite $LaMgAl_{11}O_{19}$ by simultaneously substituting La^{3+}, Mg^{2+} and Al^{3+} ions with large ionic radius Ba^{2+}, Zn^{2+} and Ti^{4+} (Table S1, Supplementary information), respectively, and introducing nanostructure and layered microstructures through citric acid sol-gel route[19] and spark plasma sintering technique[20]. A better understanding of the influences of point defects, nano-grain boundaries and layered structures on thermo-physical properties is obtained by combining experimental results with the calculated minimum thermal conductivity using Clarke's model[21,22]. The results demonstrate that the thermal conductivities of $La_{1-x}Ba_xMg_{1-x}Zn_xAl_{11-x}Ti_xO_{19}$ (LBMZATO, x = 0.0, 0.1, 0.2, 0.3, 0.4, 0.5) ceramics are exceptionally low, close to the predicated minimum thermal conductivities, which verifies that the inter-atomic spacing-sized phonon mean free paths are responsible for the point-defect scattering, high-denstiy grain-boundary scattering, and localized phonon vibrational modes by layered crystal structure. More importantly, the coefficients of thermal expansion of LBMZATO ceramics at 1073–1273 K also show a remarkable improvement with the increased Ba^{2+}, Zn^{2+} and Ti^{4+} content fraction, reaching the maximal value of 11.39×10^{-6} K^{-1} at 1273 K, which is close to the CTE of 7 ~ 8 wt.% yttria stabilized zirconia (YSZ) system at the elevated temperature[23]. These conclusions suggest that LBMZATO ceramics are promising candidates for advanced thermal barrier coatings applications.

Results

According to the XRD patterns (Fig. S2), all the obtained LBMZATO ceramics were comprised of pure magnetoplumbite $LaMgAl_{11}O_{19}$ phase. Increasing $Ba^{2+} + Zn^{2+} + Ti^{4+}$ doping fraction leads to a shift of the X-ray spectra to lower 2θ values (Fig. S3). The refined cell parameters of LBMZATO (with $0.0 \leq x \leq 0.5$) are reported in Table S2. The sites formation energy calculation of invasion ions and host ions in $La_{1-x}Ba_xMg_{1-x}Zn_xAl_{11-x}Ti_xO_{19}$ series were calculated by material stuido (Tab. S3). The exact composition of the materials were determined by X-ray fluorescence spectrometry (XRF, Tab. S4) and X-ray photoelectron spectroscopy (XPS, Tab. S5 and Fig. S4). It can be concluded that Ba^{2+}, Zn^{2+} and Ti^{4+} have completely entered the sites of La^{3+}, Mg^{2+} and Al^{3+}, respectively, and finite solid solutions have formed. For the magnetoplumbite $LaMgAl_{11}O_{19}$, the dependence between parameters of LBMZATO and Ba^{2+}, Zn^{2+} and Ti^{4+} doping fraction was approximately consistent with the Vegard's law[24], which displays a linear relationship between crystal structural parameters and composition variation. The smallest platelike crystallites in this material were 35 nm in thickness, as clearly evidenced in the typical SEM image of $LaMgAl_{11}O_{19}$ without doping (Figure 1a). Figure 1b is the typical TEM morphology of $LaMgAl_{11}O_{19}$ showing uniformity of phase composition. The selected area electron diffraction (SAED) pattern (Figure 1c) confirms that $LaMgAl_{11}O_{19}$ possesses a magnetoplumbite-type hexagonal crystal structure. High resolution TEM (HRTEM) image (Figure 1d) with electron beam parallel to $[\bar{1}\ \bar{1}\ 21]_{LaMgAl_{11}O_{19}}$ direction also revealed the crystalline structure and the smooth surface with a $(1\ \bar{1}\ 00)$ plane.

As observed in the high-magnification SEM and TEM (Figure 2a,b), stepped crystal grains with ~50 nm height and ~100 nm width exist in the sample. Figure 2 (c) is a high-magnification atomic resolution image in [0001] direction, which reveals two parts that are separated by one dashed line. Figure 2d is the reduced FFT(Fast Fourier Transform) from region B in Figure 2c, including two clear step-like surfaces. The electron diffraction patterns of the upper and lower parts show identical magnetoplumbite-type hexagonal crystal structure. Detailed analysis showed that the lower and upper parts were well matched with each other because both include (004) and (006) lattice planes, which indicates that the borderline between the lower and upper parts is coherent interface.

The thermal diffusivities and specific heat capacities in the range 293–1273 K are illustrated in Fig. S5 and Fig. S6 (Tab. S6), respectively. The thermal conductivities initially decrease with increasing x, reaching their lowest values at $x = 0.5$. The thermal conductivity of LBMZATO decreases with increasing temperature from room temperature to 800°C (Figure 3). Due to thermal radiation at high temperatures, thermal conductivity becomes less sensitive to composition variation, instead, it rises slightly. The T^{-1} temperature-dependent thermal conductivity for LBMZATO suggests a dominant phonon conduction behavior in most inorganic non-metallic materials. Thermal conductivities of LBMATO ceramics are obviously lower than 8YSZ, especially for $La_{0.5}Ba_{0.5}Mg_{0.5}Zn_{0.5}Al_{10.5}Ti_{0.5}O_{19}$, whose thermal conductivity values are 1.51 ~ 1.67 $W \cdot m^{-1} \cdot K^{-1}$ from room temperature to 1000°C. The coefficients of thermal expansion of LBMZATO (with $0.0 \leq x \leq 0.5$) solid solution are plotted in Figs. S7–8. CTE rises with the increasing Ba^{2+}, Zn^{2+} and Ti^{4+} fraction, which exhibits a composition dependence similar to the reverse composition dependence of the thermal conductivity.

Discussion

An inter-atomic spacing-sized phonon mean free path means that the strongest scattering occurs in the crystal cell and corresponds to the minimum thermal conductivity as reported by Clarke[21]. In light of Debye's phonon gas theory, thermal conduction in dielectric solids can be considered as the transport of phonons carrying energy, and the thermal conductivity of materials is then represented in another form equivalent to $\kappa = \alpha \cdot C_p \cdot \rho$, by the relation[25]:

$$\kappa' = \frac{1}{3} C_V \cdot v_m \cdot l, \tag{3}$$

where C_V, v_m and l represent the heat capacity per unit volum, the average speed of sound in the materials and the phonon mean free path, repectively. By combining Eqs (3) and the relation $C_V = C_p \cdot \rho$, the phonon mean free path can be expressed as:

$$l = \frac{3\alpha}{v_m} \tag{4}$$

where α is characterized by the laser flash system (Netzsch LFA 427, Germany) from room temperature up to 1273 K in an argon atmosphere. For each temperature, three measurements were made to obtain the mean value of thermal diffusivity. The average speed of sound v_m is determined by the relation:

$$v_m = \left[\frac{3(v_t v_l)^3}{2v_l^3 + v_t^3}\right]^{1/3} \tag{5}$$

Combining Eqs.(4) and (5), the phonon mean free path can be obtained:

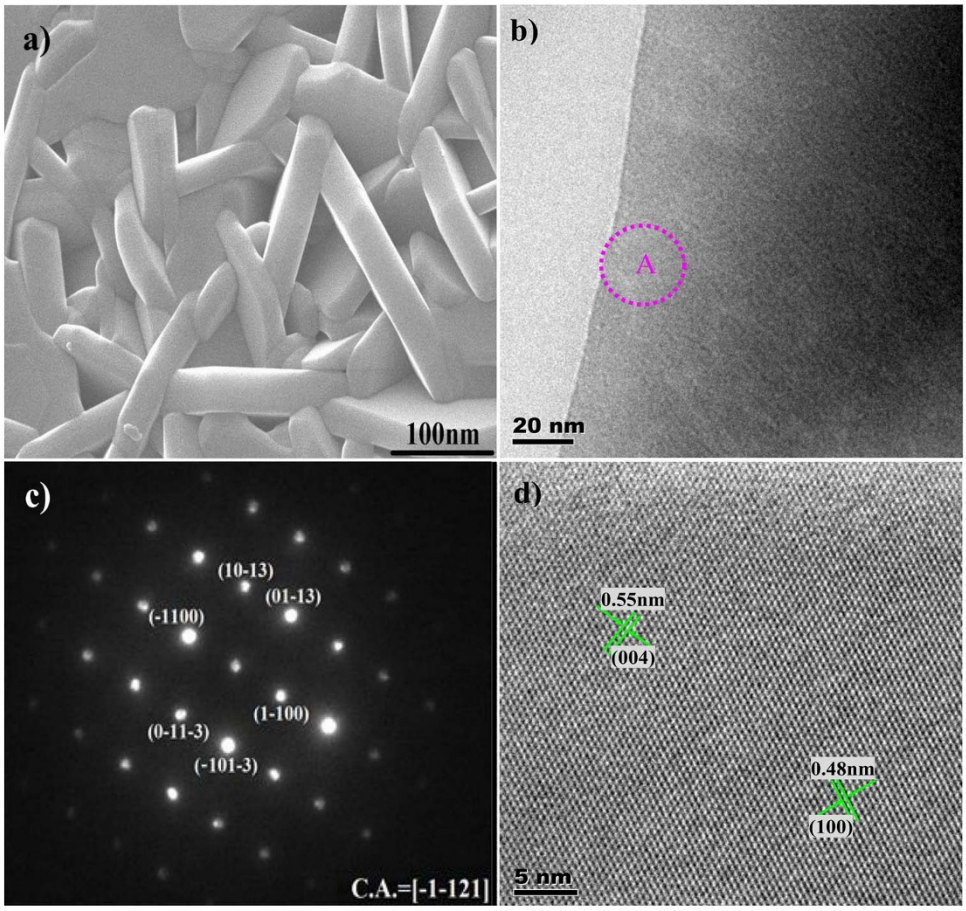

Figure 1 | (a) The scanning electron microscope (SEM image) for mother material $LaMgAl_{11}O_{19}$, sintered by spark plasma sintering(SPS) technique at 1500°C for 10 min. (b) TEM characterizations of the mother material $LaMgAl_{11}O_{19}$.(c) The corresponding selected area electron diffraction (SAED) patterns taken from the red circle region A in (b). (d) The HRTEM image taken from the middle region A in (b).

$$l = 3\alpha/3^{1/3}\left(\frac{1}{v_l^3} + \frac{2}{v_t^3}\right)^{-1/3} \tag{6}$$

where v_l and v_t represent longitudinal and transverse sound speed, repectively.

The phonon mean free path of LBMZATO solid solutions as a function of temperature is plotted in Fig. 4. The phonon mean free paths of LBMZATO are nearly temperature-independent above 873 K (equal to Debye temperature of LBMZATO), which agrees with the typical behavior of inorganic materials. The phonon mean free paths of LBMZATO ceramics vary between 0.18 and 0.34 nm in the range from room temperature to 1000°C. This confirms that the phonon mean free path is smaller than parameters ($a = b = 5.5920$ Å, $c = 21.9650$ Å) and approaches the inter-atomic spacing. The distance between the Al^{3+} cation and O^{2-} anion in AlO_5 hexahedron is 1.74 Å[26].

Clarke evaluated a formula based on the minimum thermal conductivity according to the phonon mean free path equal to the inter-atomic spacing[20]:

$$k_{\min} = 0.87 k_B N_A^{2/3} \frac{m^{2/3}\rho^{1/6}E^{1/2}}{M^{2/3}} \tag{7}$$

where k_B is Boltzmann's constant, N_A is the Avogadro number, m is number of atoms per molecule, ρ is the density, M is the molecular mass, and E is the Young's modulus. Values of $k_{\min}$ were calculated by Eq.(7) and the relationship between $k_{\min}$ and composition was also plotted in Fig. 3. The measured thermal conductivity of LBMZATO was close to the calculated minimum thermal conductivity, which means that the phonon mean free path may be as small as the inter-atomic spacing.

With the aid of the Debye model, the mechanism behind the such low thermal conductivities in LBMZATO solid solution can be well understood. The thermal conductivity in the form of the Debye model could be given by[27,28]:

$$\kappa_L = \frac{k_B}{2\pi^2 v}\left(\frac{k_B T}{\hbar}\right)^3 \int_0^{\Theta_D/T} \frac{x^4 e^x}{\tau_C^{-1}(e^x-1)^2} dx \tag{8}$$

where $x = \hbar\omega/(k_B T)$ is a dimensionless quantity and τ_C is the phonon scattering relaxation time. The following processes are assumed to limit the flow of phonons: grain-boundary scattering, point-defect scattering, phonon-phonon Umklapp scattering, stacking faults and dislocation. Therefore the combined resistive τ_C^{-1} (reciprocal of relaxation time) can be defined[29,30]:

$$\begin{aligned}\tau_C^{-1} &= \tau_B^{-1} + \tau_D^{-1} + \tau_P^{-1} + \tau_S^{-1} + \tau_{Dis}^{-1} + \tau_{Stepped}^{-1} \\ &= \frac{v_m}{L} + A\omega_D^4 + B\omega_D^2 T e^{-\Theta_D/3T} + C\left(\frac{2\gamma^2 V^{1/3}}{27v}\right)\omega_D^2 + D\omega_D + E\omega_D^2\end{aligned} \tag{9}$$

where τ_B^{-1}, τ_D^{-1}, τ_P^{-1}, τ_S^{-1}, τ_{Dis}^{-1} and $\tau_{Stepped}^{-1}$ are the resistives contributed by grain-boundary scattering, point-defect scattering, phonon-phonon Umklapp scattering and grain-boundary scattering, stacking faults, dislocation and stepped surface, respectively. L is the typical grain size and A, B, C, D and E are adjustable parameters for phonon scattering from point-defect, Umklapp phonon-phonon interactions, stacking faults, dislocation, and displacement layers respectively. In this work, authors suppose that the main sources of thermal

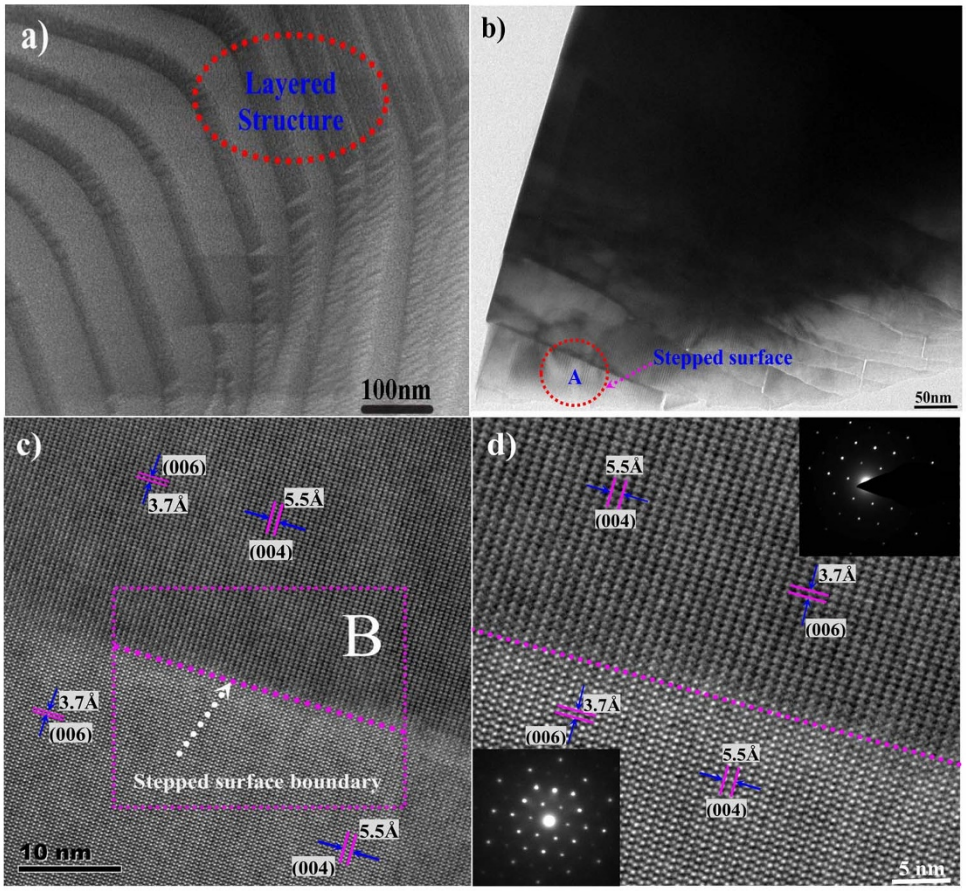

Figure 2 | (a) The high-magnification SEM image for LBMZATO with Ba^{2+}, Zn^{2+} and Ti^{4+} dopant content fraction $x = 0.3$. (b) The high-magnification transmission electron microscope (TEM) image of (a). (c) The HRTEM image taken from the red circle region A in (b). (d) The reduced FFT from region B in image (c) includes two clear step-like surfaces.

resistance are represented by plate-like grain boundary[31,32] and point-defect[33] as well as stepped surface[10,34] in the crystal. The grain boundary term has the least effect on the phonon mean free path in conventional coarser-grained materials. However, the phonon mean-free-path may be strongly affected by the additional phonon scattering at interfaces that is induced by grain-size reduction[35,36]. In our study, it is hypothesized that nanocrystalline materials offer the potential of limiting thermal conductivity by incorporating plate-like grain boundary scattering as an extrinsic phonon-scattering phenomenon. The expression for relaxation time due to grain boundary scattering process has been given by Casimir[37]:

$$\tau_B^{-1} = \frac{v_m}{L} \tag{10}$$

where v_m is the mean velocity of phonons in the material, L mean grain size. Due to enhanced phonon scattering at high-density grain boundaries (Fig. 5a), the specimens synthesized by citric acid sol-gel technique showed a reduction (~13%) in thermal conductivity compared with the conventional solid-state with microscale grains (Fig. 5b).

The resistive contributed by point-defect scattering can be given by Klemens as[38]:

$$\tau_D^{-1} = A\omega_D^4 = \frac{1}{4\pi}\left(\frac{\delta}{v_m}\right)^3 \Gamma\omega_D^4 \tag{11}$$

where Γ is the total imperfection parameter, which is given in Eqs.(S1–3, Supporting Information). Debye frequency ω_D is given by $(6\pi^2 v_m^3/\Omega)^{1/3}$, where Ω is given by M_A/ρ, M_A is the average atomic mass and M_A of $LaMgAl_{11}O_{19}$ is 3.96×10^{-23} g.

In addition, authors consider another process of phonon scattering in LBMZATO samples to account for the resistive contributed by stepped surface $\tau_{Stepped}^{-1}$[39]:

$$\tau_{\text{Stepped}}^{-1} = E\omega_D^2 = \frac{4}{3}\frac{1}{G_N v_m}\frac{a}{18}\gamma^2\omega_D^2 \tag{12}$$

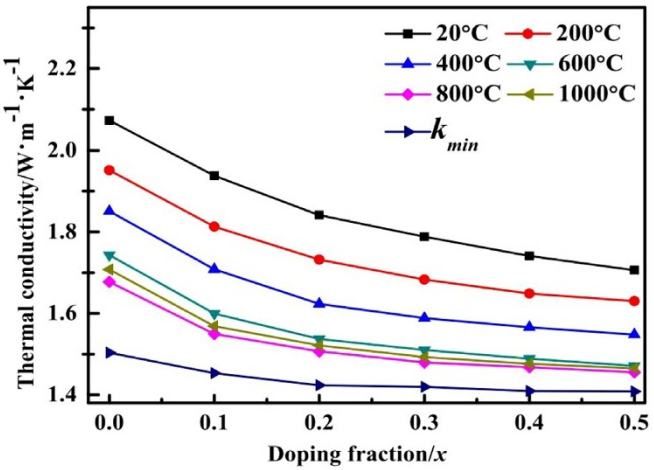

Figure 3 | **Thermal conductivity as a function of temperature for fully dense LBMZATO ($0.0 \le x \le 0.5$) ceramics.** The standard deviation of thermal conductivity values is within 2% based on three independent laser flash measurements, which is smaller than the symbol in the figure.

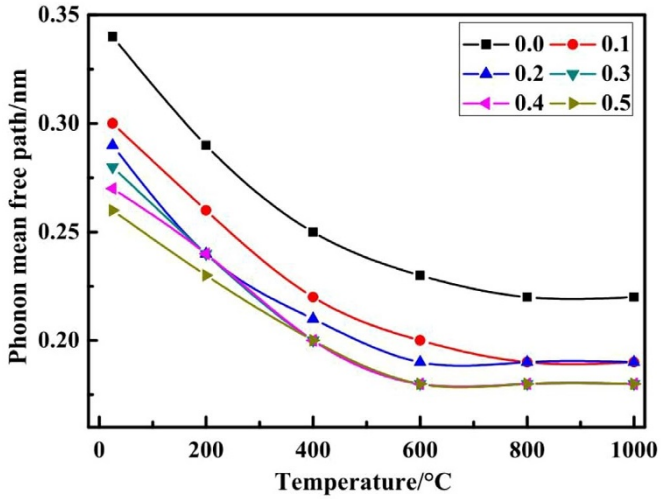

Figure 4 | Phonon mean free path of LBMZATO ($0.0 \leq x \leq 0.5$) ceramics as a function of temperature.

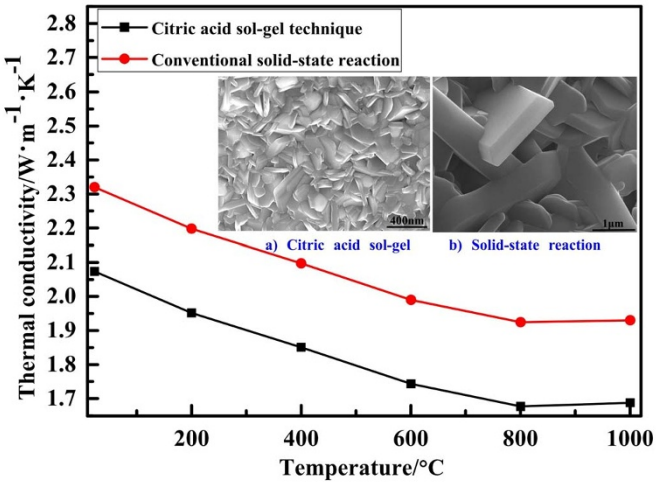

Figure 5 | The comparison of thermal conductivity for fully dense $LaMgAl_{11}O_{19}$ ceramics synthesized by conventional solid-state reaction and citric acid sol-gel technique. The standard deviation of thermal conductivity values is within ±2% based on three independent laser flash measurements, which is smaller than the symbol in the figure.

where G_N is the number of stepped surface in a crystal, a is the constant. Vibrations of stepped surfaces have been studied by P. Knipp[40,41]. In the proximity of a step, further reduction of atomic coordination induces even more charge-density redistribution and a more substantially altered interatomic potential than for a flat surface. Numerical studies show that the characteristics of surface modes depend strongly on the surface interatomic potential. The main difference between the phonon structures of the vicinal surfaces and the unstepped surface lies in the shape of their Brillouin zones. The polarizations of the step phonons change from row to row, but a stepped phonon is strictly longitudinal and the other two are strictly transverse at the step edge, where the amplitudes are maximum[42]. P. Knipp[40] reported the existence and characteristics of edge-localized vibrational modes for the simplest model by fcc surface dynamics. Though somehow speculative, authors consider the number of stepped surfaces in a crystal is proportional to the Ba + Zn + Ti concentration (Fig. 6). Authors consider the mechanism behind morphology change is due to the two dimensional nucleationstep mechanism of crystal growth in Ln-Me-A sites co-substituted $LnMeA_{11}O_{19}$ ceramics. The nucleation type is determined by the thermal roughness of crystal surface, which is determined by the relation[43]:

$$\gamma = (2\phi_{ff} + 2\phi_{ss} - 4\phi_{sf})/k_B T \qquad (13)$$

where ϕ_{ff}, ϕ_{ss} and ϕ_{sf} represent the interaction energy between the average contents of two neighboring blocks of fluid, the potential energy of a solid-solid nearest-neighbor pair and the average potential energy of a solid-fluid pair, repectively, k_B is Boltzmann's constant. The thermal roughness of crystal surface γ rises with the increasing Ba^{2+}, Zn^{2+} and Ti^{4+} fraction in $La_{1-x}Ba_xMg_{1-x}Zn_xAl_{11-x}Ti_xO_{19}$ system. When γ is greater than the critical value of 4, the nucleation mechanism is transformed from normal growth to two dimensional nucleation growth. Therefore, the number of stepped surfaces in Ba-Zn-Ti co-doped $LaMgAl_{11}O_{19}$ system increases with the increasing dopant fraction.

The calculated relaxation times due to grain boundaries, point defects and stepped surfaces in LBMZATO based on Eqs. (10–12) are plotted in Fig. 7. It can be seen from Fig. 7 that both the τ_D and $\tau_{Stepped}$ contributed by point-defects and stepped surfaces, respectively, decrease with the Ba + Zn + Ti concentration varying from $x = 0.1$ to 0.5. It is evident that by forming solid solutions of LBMZATO substantial additional resistive of the phonons flow is introduced in suppressing the thermal conductivity. Here the current authors provided a novel thought to find some new microstructure optimization processes to further lower thermal conductivity for thermal barrier coatings, such as materials with stepped surface to localize phonon vibrational modes or nano-platelet-like structure to incorporate additional grain boundary scattering.

In summary, this study on Ba^{2+}, Zn^{2+} and Ti^{4+} co-doped Lanthanum magnesium aluminate $LaMgAl_{11}O_{19}$ ceramics displays increased CTE and reduced thermal conductivity, which is contributed by the substantial additional point-defect scattering, plate-like grain-boundary scattering, and stepped surfaces. Point defects are effective at scattering short wavelength phonons, while plate-like nano-grains are required to scatter mid- and long-wavelength phonons effectively, highl-density grain boundaries and layered microstructures can play an effective role in scattering longer-wavelength phonons. A novel thought to further lower thermal conductivity was provided by introducing multi-enhanced-phonon scattering modes in Ln-Me-A sites co-substituted $LnMeA_{11}O_{19}$ ceramics, namely, materials with stepped surface to localize phonon vibrational modes and point defect mechanism, as well as nano-platelet-like structure to incorporate additional grain boundary scattering. A low thermal conductivity of 1.44 ~ 1.65 $W \cdot m^{-1} \cdot K^{-1}$ at 1027 K qualifies the $LaMgAl_{11}O_{19}$ based-bulk ceramics with high CTE (~11.2 × 10^{-6} K^{-1}, T = 1027 K) as a promising candidate for advanced thermal barrier coatings.

Methods

The series of samples were synthesized through citric acid sol-gel route over the solid solution range according to the formula $La_{1-x}Ba_xMg_{1-x}Zn_xAl_{11-x}Ti_xO_{19}$ (LBMZATO, x = 0.0, 0.1, 0.2, 0.3, 0.4, 0.5). Details of powder processing approach used in citric acid sol-gel route are described elsewhere[44]. The acquired powders were isostatically cool pressed, and sintered at 1500°C for 6 h in air to obtain LBMZATO ceramics. The LBMZATO ceramics were machined into samples of 5.0 × 5.0 × 20.0 mm for CTE characterization. Finally, full dense LBMZATO ceramics were prepared by spark plasma sintering under an applied pressure of 50 MPa at 1500°C with a constant heating rate 100°C min^{-1} to mold into pellets of ~12.7 mm in diameter and ~1.2 mm in thickness. The temperature remained at 1500°C for 15 min and a constant vacuum pressure of 4.5 Pa was maintained throughout the entire sintering process. As the specimens were loaded into a graphite die with an internal diameter of 13.1 mm, the LBMZATO changed into black disks due to the presence of excess graphite so all of the specimens were further heated in air at 950°C for 8 h. The phase compositions of the sintered pellets were identified by X-ray diffraction (XRD) (Bruker-D8 Advance Da Vinci) with CuKα radiation (40 mA, 40 kV) with 2θ angle range from 10 to 90°. The phase structure were identified using a Raman spectrometer (Raman, LabRAM HR800, HORIBA Jobin Yvon, France) using an argon ion laser with radiation at 633 nm, and collected across wavenumbers 400 ~ 2000 cm^{-1}. The signal was collected at a rate of 600 cm^{-1}/30 s and accumulated by triple scanning. The sound speed in each of the solid solutions was measured by an

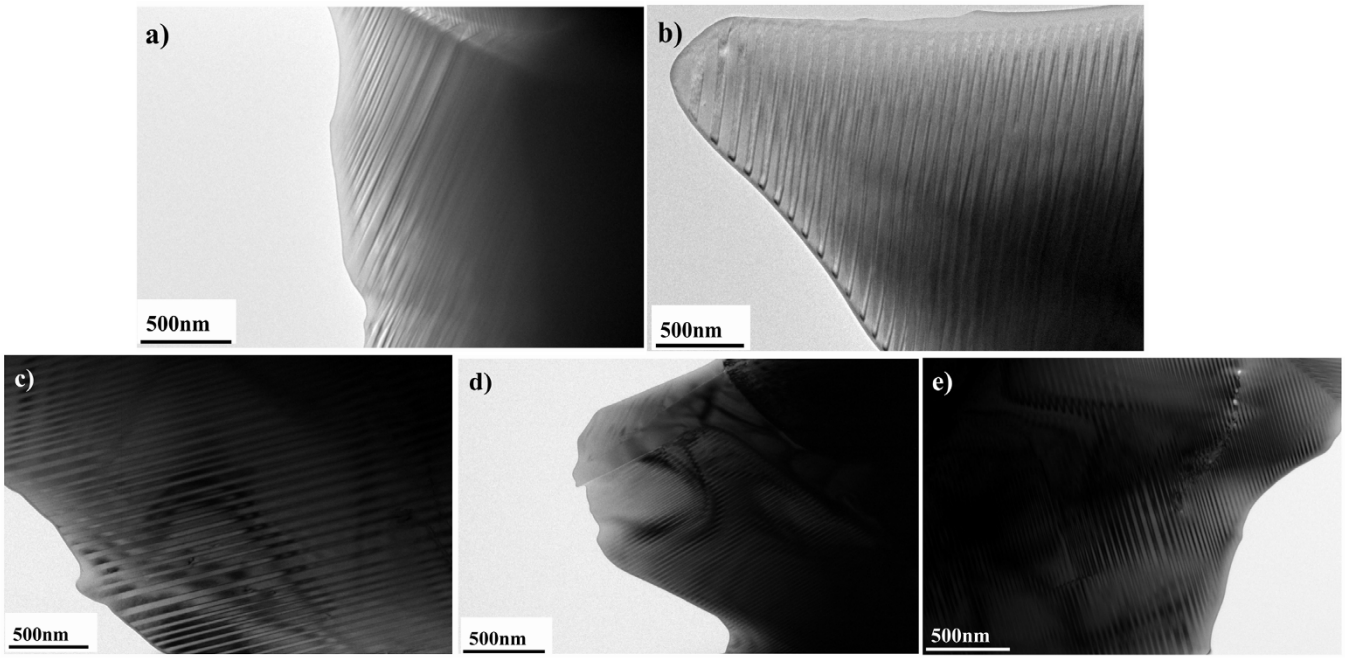

Figure 6 | The high-magnification transmission electron microscope (TEM) image of LBMZATO with stepped surfaces. (a) $x = 0.1$; (b) $x = 0.2$; (c) $x = 0.3$; (d) $x = 0.4$; (e) $x = 0.5$.

ultrasonic reflection method with a computer controlled ultrasonic pulser-receiver (Olympus Model 5073PR, Waltham, MA, USA). The morphology and crystal structure in LBMZATO phases upon Ba^{2+} + Zn^{2+} + Ti^{4+} co-substitution were evaluated by field emission scanning electron microscopy (SEM, JSM-7001F, JEOL, Japan) and high resolution transmission electron microscopy/electron diffraction (HRTEM/ED, JEM-2010F, JEOL, Japan) techniques.

The thermal diffusivities of the samples were characterized by the laser flash system (Netzsch LFA 427, Germany) from room temperature up to 1273 K exposed to air, and the temperature rise at the back side is measured as a function of time with an In-Sb infrared detector. The front and the back surfaces of each specimen were coated with two thin layers of carbon, approximately 10 μm thick, both to ensure the laser absorption at the front surface and to standardize the absorptance of the front surface and the emissivity of the back surface of the specimen. For each temperature three measurements were made to obtain the mean value of thermal diffusivity. The error in thermal diffusivity tests is within ±2%. The specific heat capacitances of the solid solutions at various temperatures were calculated according to the Neumann-Kopp rule based on the reference specific heat values of La_2O_3, BaO, MgO, ZnO, Al_2O_3 and TiO_2. The real densities of the LBMZATO ceramics were measured by Archimedes' method. The thermal conductivity (κ) was calculated from the measured diffusivity ($a/mm^2 \cdot s^{-1}$), the specific heat ($C_p/J \cdot g^{-1} \cdot K^{-1}$) and the density ($\rho/g \cdot cm^{-3}$) using the relationship:

$$\kappa = \rho \cdot C_p \cdot \alpha, \tag{14}$$

The thermal conductivity of the full dense solid, κ_f, was further normalized by the formula[45]:

$$\frac{\kappa}{\kappa_f} = 1 - \frac{4}{3}\phi, \tag{15}$$

where Φ is the porosity of the sintered specimen.

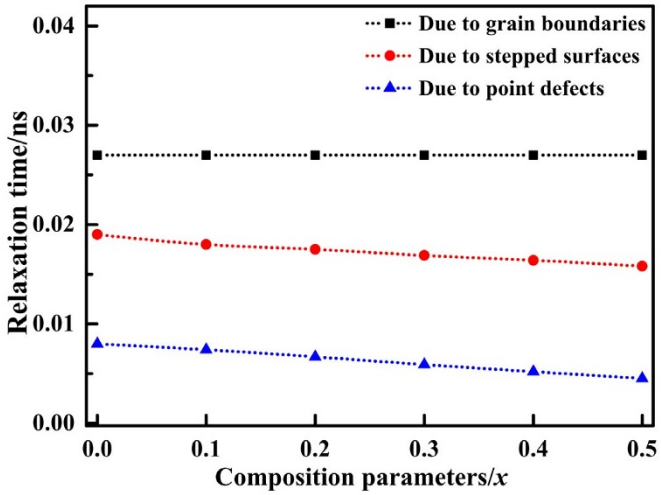

Figure 7 | The calculated relaxation times due to grain boundaries, point defects and stepped surfaces as a function of the Ba + Zn + Ti concentration in LBMZATO solid solution(ω_D = 5.87 × 10^{13} Hz, T = 300 K).

1. Slack, G. A. Nonmetallic crystals with high thermal conductivity. *J. Phys. Chem. Solids.* **34**, 321–335 (1973).
2. Kim, W. *et al.* Thermal conductivity reduction and thermoelectric figure of merit increase by embedding nanoparticles in crystalline semiconductors. *Phys. Revi. Lett.* **96**, 045901–4 (2006).
3. Peterson, R. B. Direct simulation of phonon-mediated heat transfer in a Debye crystal. *J. Heat Transfer.* **116**, 815–822 (1994).
4. Lehmann, H., Pitzer, D., Pracht, G., Vassen, R. & Stöver, D. Thermal Conductivity and Thermal Expansion Coefficients of the Lanthanum Rare-Earth-Element Zirconate System. *J. Am. Ceram. Soc.* **86**, 1338–1344 (2003).
5. Clarke, D. R. & Phillpot, S. R. Thermal barrier coating materials. *Mater. Today* **8**, 22–29 (2005).
6. Schlichting, K. W., Padture, N. P. & Klemens, P. G. Thermal conductivity of dense and porous yttria-stabilized zirconia. *J. Mater. Sci.* **36**, 3003–3010 (2001).
7. Bansal, N. P. & Zhu, D. M. Thermal properties of oxides with magnetoplumbite structure for advanced thermal barrier coatings. *Surf. Coat. Technol.* **202**, 2698–2703 (2008).
8. Pracht, G., Vafien, R. & Stover, D. Lanthanum-Lithium Hexaaluminate—A New Material for Thermal Barrier Coatings in Magnetoplumbite Structure—Material and Process Development. Adv. Ceram. Coat. Interfaces:Ceram. *Eng. Sci. Proc.* **27**, 87–99 (2008).
9. Costescu, R. M. *et al.* Ultra-low thermal conductivity in W/Al_2O_3 nanolaminates. *Sci.* **303**, 989–990 (2004).
10. He, J. Q. *et al.* Strong Phonon Scattering by Layer Structured $PbSnS_2$ in PbTe Based Thermoelectric Materials. *Adv. Mater.* **24**, 4440–4444 (2012).
11. Feser, J. P. *et al.* Ultralow Thermal Conductivity in Polycrystalline CdSe Thin Films with Controlled Grain Size. *Nano Lett.* **13**, 2122–2127 (2013).
12. Vineis, C. J. *et al.* Nanostructured Thermoelectrics: Big Efficiency Gains from Small Features. *Adv. Mater.* **22**, 3970–3980 (2010).
13. Lan, J. L. *et al.* Enhanced Thermoelectric Properties of Pb-doped BiCuSeO Ceramics. *Adv. Mater.* **25**, 5086–5090 (2013).
14. Zhao, L. Y. *et al.* Peierls distortion as a route to high thermoelectric performance in $In_4Se_{3-\delta}$ crystals. *Nature* **459**, 965–968 (2009).

15. Park, J. G. & Cormack, A. N. Defect structures and nonstoichiometry in lanthanum hexa-aluminate. *J. Eur. Ceram. Soc.* **19**, 2249–2256 (1999).
16. Iyi, N., Inoue, Z., Takekawa, S. & Kimura, S. The Crystal Structure of Lanthanum Hexaaluminate. *J. Solid. State. Chem.* **54**, 70–77 (1984).
17. Gasperin, M., Saine, M. C., Kahn, A., Laville, F. & Lejus, A. M. Influence of M^{2+} Ions Substitution on the Structure of Lanthanum Hexa-aluminates with Magnetoplumbite Structure. *J. Solid State Chem.* **54**, 61–69 (1984).
18. Cao, X. Q., Vassen, R. & Stoever, D. Ceramic materials for thermal barrier coatings. *J. Eur. Ceram. Soc.* **24**, 1–10 (2004).
19. Mali, A. & Ataie, A. Structural characterization of nano-crystalline $BaFe_{12}O_{19}$ powders synthesized by sol–gel combustion route. *Scripta Mater.* **53**, 1065–1070 (2005).
20. Hungrí, T., Galy, J. & Castro, A. Spark plasma sintering as a useful technique to the nanostructuration of piezo-ferroelectric materials. *Adv. Eng. Mater.* **11**, 615–631 (2009).
21. David, R. Clarke. Materials selection guidelines for low thermal conductivity thermal barrier coatings. *Surf. Coat. Technol.* **163–164**, 67–74 (2003).
22. Clarke, D. R. & Phillpot, S. R. Thermal barrier coating materials. *Mater. Today* **8**, 22–29 (2005).
23. Hayashi, H. *et al*. Thermal Expansion Coefficient of Yttria Stabilized Zirconia for Various Yttria Contents. *Solid State Ionics* **176**, 613–619 (2005).
24. Mitsui, T. & Westphal, W. B. Dielectric and X-Ray Studies of $Ca_xBa_{1-x}TiO_3$ and $Ca_xBa_{1-x}TiO_3$. *Phys. Rev.* **124**, 1354–1359 (1961).
25. Jackson, H. E. & Walker, C. T. Thermal Conductivity, Second Sound, and Phonon-Phonon Interactions in NaF. *Phys. Rev. B* **3**, 1428–39 (1971).
26. Smith, J. V. A review of the Al-O and Si-O distances. *Acta Cryst.* **7**, 479–481 (1954).
27. Holland, M. G. Analysis of thermal conductivity. *Phys. Rev.* **132**, 2461–2471 (1963).
28. Callaway, J. Model for thermal conductivity at low temperatures. *Phys. Rev.* **113**, 1046–1051 (1959).
29. Callaway, J. & von Baeyer, H. C. Effect of point imperfections on thermal conductivity. *Phys. Rev.* **120**, 1149–1154 (1960).
30. Zhou, Z., Uher, C., Jewell, A. & Caillat, T. Influence of point-defect scattering on the thermal conductivity of solid solution Co $(Sb_{1-x}As_x)_3$. *Phys. Rev. B* **71**, 235209–6 (2005).
31. Nicholls, J. R., Lawson, K. J., Johnstone, A. & Rickerby, D. S. Methods to reduce the thermal conductivity of EB-PVD TBCs. *Surf. Coat. Tech.* **151**, 383–391 (2002).
32. Rowe, D. M., Shukla, V. S. & Savvides, N. Phonon scattering at grain boundaries in heavily doped fine-grained silicon–germanium alloys. *Nature* **290**, 765–766 (1981).
33. Lu, H. R., Wang, C. A. & Zhang, C. G. Influence of Ln^{3+} and B^{3+} Ions Co-Substitution on Thermophysical Properties of$LnMB_{11}O_{19}$-type Magnetoplumbite $LaMgAl_{11}O_{19}$ for Advanced Thermal Barrier Coatings. *J. Am. Ceram. Soc.* **96**, 1063–1066 (2013).
34. Niu, L., Gaspar, D. J. &Sibene, S. J. Phonons localized at step edges: A route to understanding forces at extended surface defects. *Sci.* **268**, 847–847 (1995).
35. Biswas, K. *et al*. High-performance bulk thermoelectrics with all-scale hierarchical architectures. *Nature* **489**, 414–418 (2012).
36. Biswas, K. *et al*. Strained endotaxial nanostructures with high thermoelectric figure of merit. *Nat. Chem.* **3**, 160–166 (2011).
37. Casimir, H. B. G. & Du Pré, F. K. Note on the thermodynamic interpretation of paramagnetic relaxation phenomena. *Physica* **5**, 507–511 (1938).
38. Klemens, P. G. Thermal resistance due to point defects at high temperatures. *Phys. Rev.* **119**, 507–509 (1960).
39. Klemens, P. G. Some Scattering Problems in Conduction Theory. *Can. J. Phys.* **35**, 441–450 (1957).
40. Knipp, P. Phonons on stepped surfaces. *Phys. Rev. B* **43**, 6908–6923 (1991).
41. Knipp, P. Surface phonons localized at step edges. *Phys. Rev. B* **40**, 7993–7995 (1989).
42. Dong, J., Sankey, O. F. & Myles, C. W. Theoretical study of the thermal conductivity in Ge framework semiconductors. *Phys. Rev. Lett.* **86**, 2361–2364 (2001).
43. Gilmer, G. H. & Bennema, P. Simulation of crystal growth with surface diffusion. *J. Appl. Phys.* **43**, 1347–1360 (2003).
44. Narottam, P. B., Zhu, D. M. & Maryam, E. G. Corrigendum to Effects of doping on thermal conductivity of pyrochlore oxides for advanced thermal barrier coatings. *Mater. Sci. Eng. A* **459**, 192–195 (2007).
45. Schlichting, K. W., Padture, N. P. & Klemens, P. G. Thermal conductivity of dense and porous yttria-stabilized zirconia. *J. Mater. Sci.* **36**, 3003–3010 (2001).

Acknowledgments

The authors would like to thank the financial support from the National Natural Science Foundation of China (NSFC–Nos.11232008 and 51221291) and Tsinghua University Initiative Scientific Research Program(No.2012THZ0).

Author contributions

H.R.L. and C.A.W. designed the experiments. H.R.L. carried out the fabrication of materials and characterization/measurement of thermo-physical properties. Y.H. contributed to microstructural characterizations. Y.H. and H.M.X. provided help in the experiments. The paper was written by H.R.L. and C.A.W., and all authors reviewed the manuscript.

Additional information

Supplementary information accompanies this paper at http://www.nature.com/scientificreports

Competing financial interests: The authors declare no competing financial interests.

How to cite this article: Lu, H., Wang, C.-A., Huang, Y. & Xie, H. Multi-Enhanced-Phonon Scattering Modes in Ln-Me-A Sites co-substituted $LnMeA_{11}O_{19}$ Ceramics. *Sci. Rep.* **4**, 6823; DOI:10.1038/srep06823 (2014).